



# InAs<sub>0.9</sub>Sb<sub>0.1</sub>-based hetero-*p-i-n* structure grown on GaSb with high mid-infrared photodetection performance at room temperature

Jinchao Tong<sup>1</sup> , Landobasa Y. M. Tobing<sup>1</sup> , Li Qian<sup>1</sup> , Fei Suo<sup>1</sup> , and Dao Hua Zhang<sup>1,\*</sup> 

<sup>1</sup> School of Electrical and Electronic Engineering, Nanyang Technological University, Nanyang Avenue, Singapore 639798, Singapore

Received: 23 March 2018

Accepted: 8 June 2018

Published online:

18 June 2018

© Springer Science+Business Media, LLC, part of Springer Nature 2018

## ABSTRACT

We present the design, fabrication, and characterization of middle-wavelength infrared photodetector based on active InAs<sub>0.9</sub>Sb<sub>0.1</sub>-based hetero-*p-i-n* structure grown on GaSb substrate. In this structure, the active absorption layer is sandwiched between thin quaternary *p*-type and *n*-type AlInAsSb layers and a heavily doped AlGaSb layer is introduced to reduce dark current. We observed good lattice matching between GaSb substrates and epitaxial layers by high-resolution X-ray diffraction. Photoluminescence (PL) spectrum at 13 K shows a full width at half maximum of  $\sim 29$  meV, demonstrating good quality active absorption layers. The band gap energy of InAs<sub>0.9</sub>Sb<sub>0.1</sub> is derived as  $\sim 0.322$  eV at 0 K by Varshni fitting from PL spectra at different temperatures. A rather flat room-temperature responsivity of  $\sim 0.8$ – $0.9$  AW<sup>-1</sup> over a wavelength range of  $\sim 2.1$   $\mu$ m is demonstrated without antireflection coating. A detectivity of  $8.9 \times 10^8$  cm Hz<sup>1/2</sup> W<sup>-1</sup> at 3.5  $\mu$ m for room-temperature operation is achieved under applied bias of  $-0.5$  V.

## Introduction

High operating temperature middle-wavelength infrared (MWIR) detectors have always been pursued for imaging applications [1]. Thermal pyroelectric and microbolometers have undergone significant progress over the past few decades, allowing infrared imagers operating at non-cryogenic environment. But their operational speed is limited by thermal response mechanisms. Much effort has been dedicated to realizing quantum-type detectors with better

responsivity and higher response speed, particularly the state-of-the-art II–VI mercury cadmium telluride (MCT/HgCdTe)-based MWIR photodetectors [2]. However, due to high Hg vapor pressure during material growth, HgCdTe-based photodetectors are known to suffer from non-uniformity and instability. On the other hand, antimony (Sb)-based III–V semiconductors have demonstrated their potential for MWIR applications. Among them, InAs<sub>1-x</sub>Sb<sub>x</sub> alloys are promising for their wide band gap tunability and good uniformity in material growth. InAsSb-based

Address correspondence to E-mail: edhzhang@ntu.edu.sg

MWIR photodetectors have been widely reported, including InAsSb photoconductors [3, 4], InAsSb/GaSb photodiodes [5], and InAsSb photovoltaic diodes [6, 7]. In device design, hetero-structures, owing to their versatile capabilities, have been widely used [8–11]. For InAsSb-based photodetection, to obtain good performance at high operational temperature, it is essential to suppress thermal currents. For this, a number of InAsSb-based device based on hetero-architectures have been proposed and realized such as nBn [12–16] with a high barrier to reduce diffusion of majority electrons, and superlattice [17–23] with less Shockley–Read–Hall (SRH) recombination. These photodetectors offer promising pathways to improve high-temperature operational performance.

In this work, we investigate the room-temperature performances of MWIR InAs<sub>0.9</sub>Sb<sub>0.1</sub>-based photodetectors with hetero-*p-i-n* architecture. Compared to conventional homojunction structure, the hetero-design with a wide band gap barrier layer can reduce the excessive dark current induced by diffusion of carriers. On the other hand, InAs<sub>0.9</sub>Sb<sub>0.1</sub> is lattice-match to GaSb, which ensures the high quality of the hetero-structure and keeps the absorption range of MWIR (3–5  $\mu\text{m}$  [24]). The quality of the structure is characterized by high-resolution X-ray diffraction (XRD). Photoluminescence (PL) spectrum at 13 K shows a full width at half maximum (FWHM) of  $\sim 29$  meV. The band gap energy of InAs<sub>0.9</sub>Sb<sub>0.1</sub> is derived as  $\sim 0.322$  eV at 0 K by Varshni law from PL spectra at different temperatures. At the operating voltage bias of  $-0.5$  to  $-0.6$  V, the photodetector exhibits a tunneling process-dominated dark bulk currents. It shows a room-temperature responsivity of  $0.91$   $\text{AW}^{-1}$  at  $3.5$   $\mu\text{m}$  under applied bias of  $-0.6$  V, corresponding to a quantum efficiency of 32.2% without antireflection (AR) coating. Room-temperature detectivity of  $8.9 \times 10^8$   $\text{cm Hz}^{1/2} \text{W}^{-1}$  is achieved at  $3.5$   $\mu\text{m}$  under applied bias of  $-0.5$  V. The results in this work enhance our understanding of high-temperature operational photodetectors and are useful for further improvements in these devices. Future work on improving the low-temperature performance will also be done.

## Materials and methods

The InAsSb-based hetero-*p-i-n* photodetector was grown on *n*-type Te-doped GaSb substrate by RIBER-32 molecular beam epitaxy (MBE) system. The band gap of GaSb at room temperature is 0.72 eV [25], which will not introduce disturbance for absorption in MWIR range. The schematic design of our photodetector and its energy band diagram are shown in Fig. 1. Different from conventional photovoltaic *p-i-n* photodetectors, we used hetero-semiconductor layers with band offsets from the *i* layer to form a *p-i-n* structure. A 1000-nm-thick *n*-type GaSb buffer layer was first grown on the *n*-type (Te:  $1.5 \times 10^{18} \text{ cm}^{-3}$ ) GaSb substrate as a contact layer for the *n*-type electrode. Afterward, 20-nm *n*-type quaternary AlInAsSb layer, 1500-nm non-intentionally doped InAs<sub>0.9</sub>Sb<sub>0.1</sub> layer (with background doping of  $< 2.1 \times 10^{15} \text{ cm}^{-3}$ ), 20-nm *p*-type AlInAsSb layer, 40-nm *p*-type AlGaSb layer, and 30-nm *p*-type AlGaSb layer with graded Al composition were grown subsequently. Finally, 30-nm *p*-type GaSb layer was grown as the

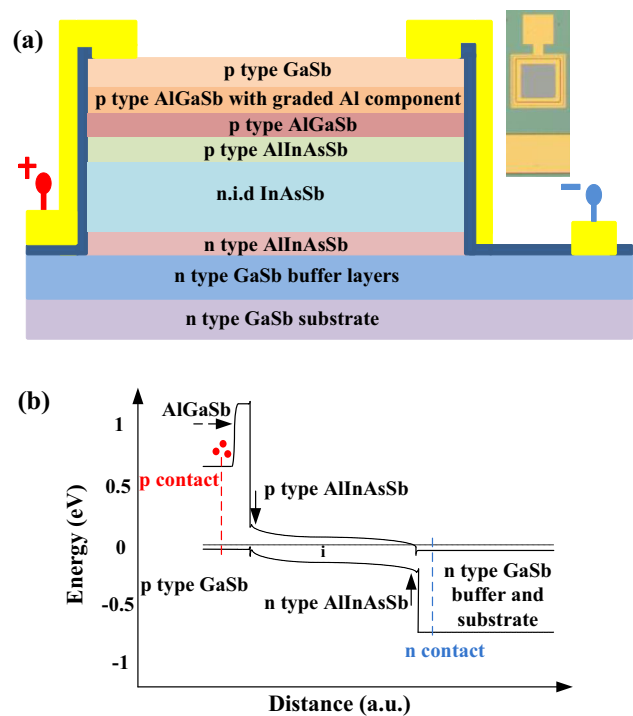


**Figure 1** **a** Cross section schematic of the photodetector (not to real scale). The right inset is typical microscope image of a 350- $\mu\text{m}$  square mesa device. **b** Schematic of the band diagram of the structure at room temperature and zero bias. The red dots represent dark electrons. For a better view, the real thickness of each layer is not reflected in this schematic.

contact layer for the *p*-type electrode. All the doped layers have a doping concentration of  $2 \times 10^{18} \text{ cm}^{-3}$  except for the top *p*-type GaSb (Be:  $\sim 1 \times 10^{18} \text{ cm}^{-3}$ ).

In our design, we attempted to reduce the high-temperature dark current originated from minority electrons in *p* sides. For this purpose, the large band gap *p*-type  $\text{Al}_x\text{Ga}_{1-x}\text{Sb}$  layer was inserted adjacent to the active  $\text{InAs}_{0.9}\text{Sb}_{0.1}$  to suppress the electron flow from *p* side. This *p*-type  $\text{Al}_x\text{Ga}_{1-x}\text{Sb}$  layer was heavily doped to reduce the minority carrier concentrations but with negligible band gap narrowing. The quaternary  $\text{AlInAsSb}$  layers inserted in *p* and *n* sides can limit type-II electron–hole transitions at the interfaces. These quaternary layers also belong to the 6.1 Å lattice constant family of III–V semiconductors such as InAs, GaSb, AlSb, and the related alloys.

Standard optical photolithography was used to define square photodetector mesas in sizes varying from 500 μm down to 20 μm. The mesas were etched down to the *n*-type GaSb buffer layer using high-temperature inductively coupled plasma-reactive ion etching (ICP-RIE), immediately followed by rinsing using  $\text{H}_2\text{SO}_4/\text{H}_2\text{O}_2/\text{H}_2\text{O}$  solution. A 300-nm-thick  $\text{SiO}_2$  layer was deposited by chemical vapor deposition (CVD) to protect the mesa. The absorption area was then defined by opening window on  $\text{SiO}_2$  using RIE. Meanwhile, a window was also opened for metal contact on the *n*-type buffer GaSb layer. Finally, Ti/Au (25/300 nm) was deposited by electron beam evaporation to form metallic contacts on the *n*-type buffer GaSb layer and *p*-type GaSb layer (Fig. 1a). A typical micrograph of a 350-μm square mesa photodetector is presented in the inset of Fig. 1a. The photodetectors were then mounted and wire-bonded to ceramic leadless chip carrier (LCC). Dark current measurements were conducted under vacuum within a liquid-nitrogen-cooled Dewar.

## Results and discussion

### Material characterization

After epitaxial growth, the quality of the materials was characterized by high-resolution X-ray diffraction (XRD) and photoluminescence (PL). Figure 2a shows the XRD spectrum of the hetero-*p-i-n* sample. It is found that the lattice mismatch between

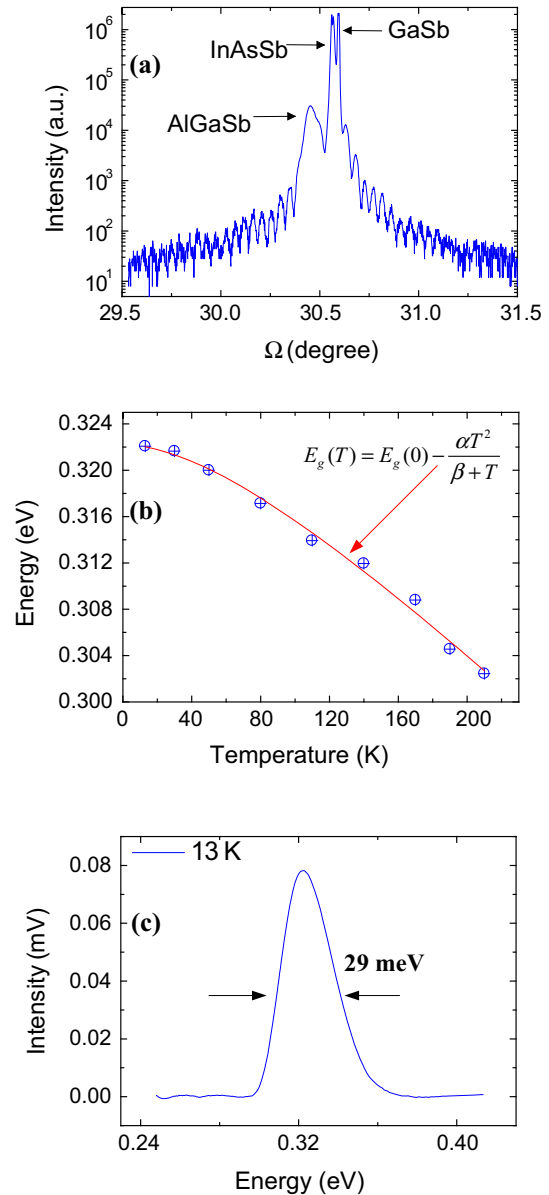


**Figure 2** **a** High-resolution XRD data (004) of the InAsSb-based hetero-*p-i-n* sample. **b** PL peak positions at different temperatures, compared to the fittings with Varshni law. **c** PL spectrum of the sample measured at 13 K.

$\text{InAs}_{0.9}\text{Sb}_{0.1}$  and GaSb substrate is 0.11%, corresponding to a Sb component of 0.1044 in InAsSb by Vegard's law, which is more than the expected 0.1. The lattice mismatch between the large band gap AlGaSb and GaSb is 0.46%, and the derived component of Al in AlGaSb is around 0.66. The optical property of the sample was characterized by PL from 13 to 210 K. The full width at half maximum (FWHM) for the PL spectrum is  $\sim 29$  meV at 13 K shown in Fig. 2c, indicating reasonable quality for the

InAs<sub>0.9</sub>Sb<sub>0.1</sub> layer. The clear and normal “red shift” of peak position with the increasing temperature is observed in Fig. 2b. The general Varshni law  $E_g(T) = E_g(0) - \alpha T^2/(\beta + T)$  is used to fit the data at  $T < 210$  K, where  $\alpha$  and  $\beta$  are two empirical parameters and  $E_g(0)$  is the energy gap at 0 K. In this range,  $E_g(0)$  is derived as 0.322 eV, which corresponds to  $\lambda = 3.851 \mu\text{m}$ .  $\alpha$  and  $\beta$  are 0.15 meV/K and 129 K, respectively. They are close to reported values [26, 27].

### Dark current characteristics

The dark current–voltage (I–V) characteristics of photodetectors with different mesa sizes were performed. For a mesa-type device, the dark current density can be expressed as  $J = I/A = (I_B + I_S)/A = J_B + J_S \cdot P/A$ , where  $I_B$  ( $J_B$ ) is the bulk dark current (density),  $I_S$  ( $J_S$ ) is the perimeter dark current (density),  $A$  is the cross-sectional area of the mesa, and  $P$  is the perimeter. Figure 3a shows the dark current density  $J$  of the photodetector under applied biases of  $-0.1$ ,  $-0.3$ , and  $-0.5$  V as a function of the perimeter-to-area ( $P/A$ ) ratio and their linear fits at room temperature at specific region. We note that at  $-0.1$  V,  $J$  increases slightly when the  $P/A$  ratio increases and the derived  $J_S$  is  $3 \times 10^{-3} \text{ A cm}^{-1}$ . Under large reverse bias,  $J$  increases faster with  $P/A$  ratio. Specifically, under the bias of  $-0.3$  V,  $J_S$  increases to  $6.8 \times 10^{-3} \text{ A cm}^{-1}$ . When the bias further increases to  $-0.5$  V,  $J_S$  increases to  $1.2 \times 10^{-2} \text{ A cm}^{-1}$ . The deviation of the data from the fitted lines at large  $P/A$  values reflects the difference in surface quality for large and small devices. It is noted that the  $J_S$  increases with the applied reverse bias, which can be attributed to the enhanced influence of the trap-assisted tunneling (TAT) as the electric field becomes stronger [28]. These results indicate large surface leakage currents in these photodetectors. In addition, we also find that by further increasing the voltage bias, the ratio between  $J_S$  and  $J_B$  ( $J_S/J_B$ ) becomes larger, indicating increased contribution of surface leakage. The large surface leakage current might originate mainly from physical damage caused in dry etching, non-ideal passivation, chemical cleanup process, gate effect from sidewalls, and the inherent issue of surface pinning of layers in the structure with high indium contents [29].

The dark current density as a function of bias voltage at different temperatures is shown in Fig. 3b

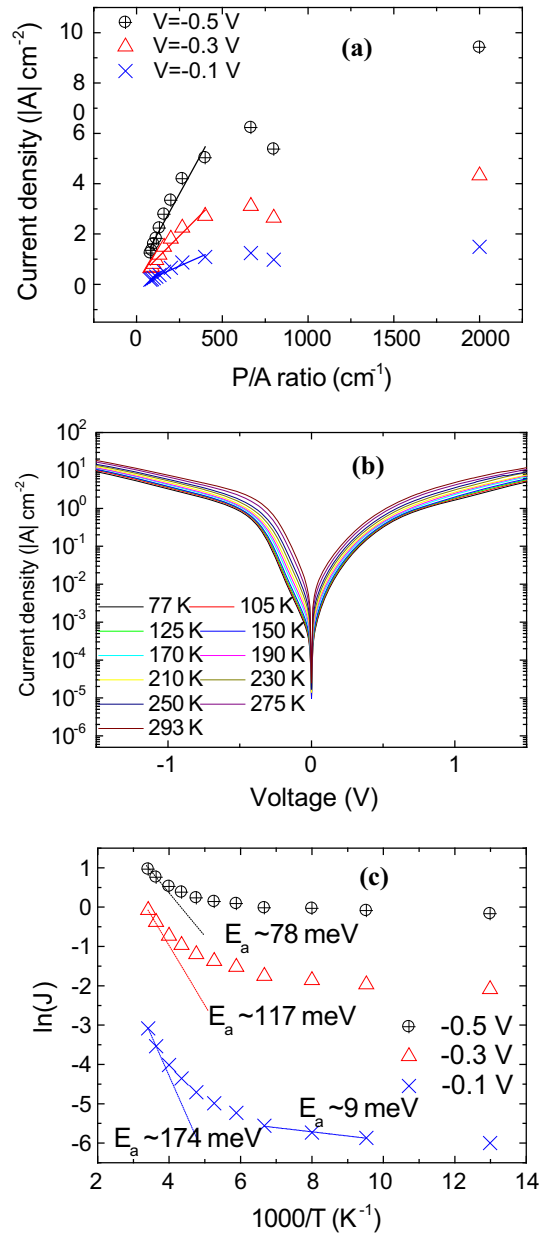


**Figure 3** **a** Dark current density versus perimeter-to-area ( $P/A$ ) ratio for photodetectors with different mesa size measured at 293 K under  $-0.1$ ,  $-0.3$ , and  $-0.5$  V bias. **b** Dark current density versus voltage for 350- $\mu\text{m}$  square mesa photodetector at different temperatures varying from 77 to 293 K. **c**  $\ln(J)$  versus  $1000/T$  for the 350- $\mu\text{m}$  square mesa photodetector under applied biases of  $-0.1$ ,  $-0.3$ , and  $-0.5$  V, combined with linear fits for the activation energy at high temperatures.

for a 350- $\mu\text{m}$  square mesa device. The dark current density is  $J = 0.848 \text{ A cm}^{-2}$  at applied bias of  $-0.5$  V and  $T = 77$  K, and increases to  $J = 2.62 \text{ A cm}^{-2}$  at  $T = 293$  K. As shown in the figure, the rectification character of this hetero- $p-i-n$  structure is not very well

and the dark current density is not reduced significantly when temperature is decreased. There is also a sharp change at around  $-0.5$  V in the slope for almost all the measured temperatures. The sharp change may come from the increased contribution of surface currents compared to bulk under large bias as indicated in Fig. 3a.

To gain an insight into the origin of bulk dark current in this hetero-*p-i-n* photodetector, we plot  $\ln(J)$  versus  $1000/T$  for the 350- $\mu\text{m}$  square mesa device under different voltages in Fig. 3c. At  $-0.1$  V, the dark current is dominated by tunneling in the lower temperature ranges ( $< 275$  K), as indicated by small activation energies [i.e., 9 meV (105–150 K)]. At temperatures higher than 275 K, the activation energy is 174 meV, which is quite close to half of the InAs<sub>0.9</sub>Sb<sub>0.1</sub> band gap value ( $E_g/2 = 161$  meV, derived from the PL measurements), indicating that the dominant dark current mechanism is Shockley–Read–Hall (SRH) recombination. This is due to a faster increase in SRH process with temperature as compared to tunneling process. The activation energy decreases very fast while increasing the voltage bias from  $-0.1$  to  $-0.3$  V (117 meV) and  $-0.5$  V (78 meV) at temperatures higher than 275 K. These results indicate that the tunneling process is dominant when the reverse voltage bias is larger than 0.1 V. At low temperatures, the saturation of  $\ln(J)$  is due to the surface leakage currents.

### Performance characterization

The spectral response of the photodetector at room temperature was characterized by a 1000 K black-body radiation source and a standard Fourier-transform infrared spectroscopy (FTIR). The structure was illuminated from the top. As shown in Fig. 4a, the photodetector has peak external quantum efficiency (QE) of  $\sim 47.8\%$  at  $\sim 2.1$   $\mu\text{m}$  under an applied bias of  $-0.6$  V. The QE decreases to  $\sim 32.2\%$  at 3.5  $\mu\text{m}$ . For a photodetector, the photocurrent responsivity  $R$  can be used to describe the photoelectric conversion efficiency. This can be expressed as  $R = \lambda q \eta / (hc)$ , where  $\lambda$  is the wavelength,  $\eta$  is the QE,  $q$  is the unit charge element,  $h$  is the Planck constant, and  $c$  is light speed in the vacuum. The responsivity  $R$  with respect to  $\lambda$  is plotted in Fig. 4b. The photodetector shows responsivity of  $\sim 0.91$   $\text{A W}^{-1}$  at 3.5  $\mu\text{m}$ , and it almost has a flat responsivity from 2.1 to 4  $\mu\text{m}$ . The

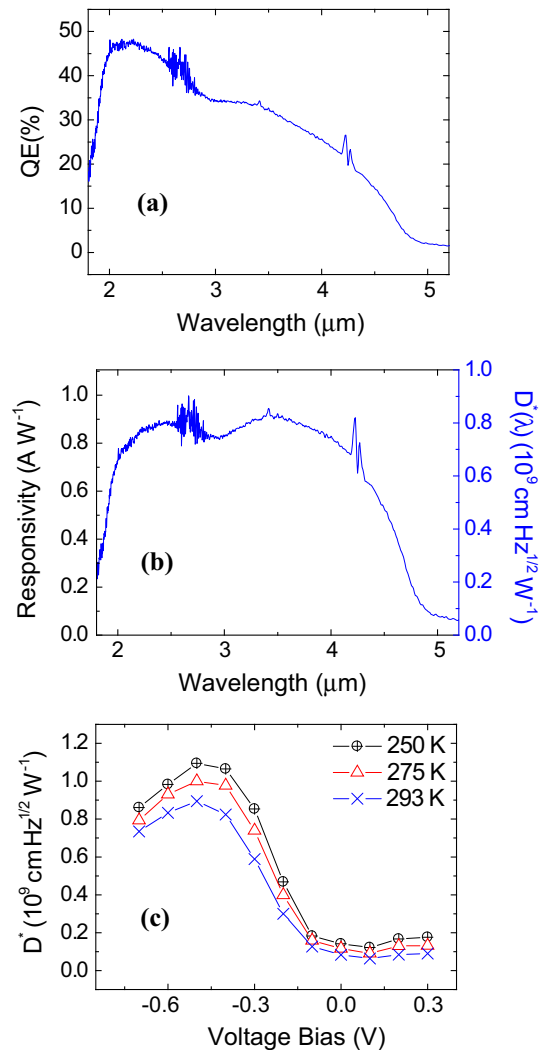


**Figure 4** **a** External QE of the photodetector for MWIR at room temperature under applied bias of  $-0.6$  V. **b** Spectral responsivity and detectivity of the photodetector at room temperature under applied bias of  $-0.6$  V. **c** Detectivity of the photodetector at room temperature (293 K), 275, and 250 K under different applied voltage bias at 3.5  $\mu\text{m}$ .

$R$  decreases very fast for wavelength larger than 4  $\mu\text{m}$ , with 100% cutoff wavelength observed around 5  $\mu\text{m}$ .

The detectivity ( $D^*$ ) defined by  $D^*(\lambda) = R(\lambda) / (2qJ + 4kT/(RA))^{1/2}$  is normally used as a figure of merit to evaluate the device performance.  $RA$  is the resistance area product, which can be derived from the  $J$ - $V$  characteristics. In this equation, dark current shot noise and Johnson noise have been included. Actually, there are two other noise contributions in our photodetectors that may affect the final performance. They are background illumination and signal



**Table 1** A summary of room-temperature performance of recently reported MWIR photodetectors

Detector type	Detectivity (cm Hz <sup>1/2</sup> W <sup>-1</sup> )
InAsSb nBn [15]	$1.0 \times 10^9$ (5.0 μm, $D^*(\lambda) = R(\lambda)/(2q(J_d + J_{ph}))^{1/2}$ )
Type-II InAs/GaSb [22]	$8.9 \times 10^8$ ( $\lambda_{C,100\%} = 6.2$ μm, blackbody $D^* = R/(4kT/(R_0A))^{1/2}$ )
InAs photovoltaic [30]	$6.1 \times 10^8$ ( $\lambda_{C,100\%} = 3.9$ μm, blackbody $D^* = R/(4kT/(R_0A))^{1/2}$ )
Type-II InAs/GaSb [21]	$8.0 \times 10^8$ (5.0 μm, $D^*(\lambda) = R(\lambda)/(4kT/(R_0A))^{1/2}$ )
Hetero-InAsSb <i>p-i-n</i> (this work)	$8.9 \times 10^8$ (3.5 μm, $D^*(\lambda) = R(\lambda)/(2qJ + 4kT/(RA))^{1/2}$ )
InAsSb photovoltaic (Hamamatsu, [31])	$9.5 \times 10^8$ (3.5 μm)

photocurrent shot noise. For the former, if we assume a background temperature of 300 K and  $2\pi$  field of view and an averaged responsivity of 0.9 A/W in 1.5–5 μm range, the background photon current density is  $\sim 7.2 \times 10^{-4}$  A cm<sup>-2</sup>. For the latter, it can be simply derived from  $RP/A$  ( $R$  is the photocurrent responsivity,  $P$  is incident power, and  $A$  is activation area), and is in the level of  $\sim 10^{-3}$ – $10^{-4}$  A cm<sup>-2</sup>. Thus, the noise contributions from these two parts can be neglected in our case due to the large dark current density (2.62 A cm<sup>-2</sup> at applied bias of  $-0.5$  V). This can be held at even smaller temperatures as the dark current does not reduce a lot. As shown, the photodetector has a detectivity of  $\sim 8.3 \times 10^8$  cm Hz<sup>1/2</sup> W<sup>-1</sup> at 3.5 μm under the bias of  $-0.6$  V. We then characterized the detectivity of the device at different bias voltages and temperatures in Fig. 4c, where the maximum detectivity at room temperature is achieved under the bias of  $-0.5$  V with a value of  $\sim 8.9 \times 10^8$  cm Hz<sup>1/2</sup> W<sup>-1</sup>. The corresponding maximum detectivities at 275 and 250 K are  $\sim 1.0 \times 10^9$  and  $\sim 1.1 \times 10^9$  cm Hz<sup>1/2</sup> W<sup>-1</sup> at the same bias. These performances are not improved a lot as the dark current, especially the surface leakage current is still very large for this detector at these temperatures. It is noted here that the detectivity shows a local maxima at reverse (negative) bias and a very low plateau at forward (positive) bias for all operational temperatures. This character originates from the dependence of detectivity on responsivity and dark current. At forward bias, the depletion area (main absorption area) is very narrow, leading to very weak responsivity, therefore low detectivity. However, while reverse bias is applied, the depletion area becomes wider, leading to increased detectivity. But as the whole intrinsic area is limited and further increasing reverse bias will increase the dark current, a maxima of detectivity at reverse bias will be appeared. Further works on

improving the quality of the material structure as well as the technical process need to do to reduce the dark current at low temperatures.

In Table 1, we summarize room-temperature performance of recently reported MWIR photodetectors as well as the commercial product. The definition of detectivity and cutoff wavelength is also tabulated for better reference. As shown, our hetero-*p-i-n* photodetector has comparable room-temperature performance to the state-of-the-art photodetectors. It is also comparable to the commonly used thermal pyroelectric detector ( $1 \times 10^9$  cm Hz<sup>1/2</sup> W<sup>-1</sup>).

### Conclusions

In summary, we have reported the design, fabrication, and characterization of InAs<sub>0.9</sub>Sb<sub>0.1</sub>-based hetero-*p-i-n* photodetectors for MWIR. Heavily doped large band gap AlGaSb electron barrier layer is inserted to limit dark current originated from electrons in p side of the structure. Quaternary AlInAsSb layers are also inserted to limit type-II contacts in the structure. The photodetector exhibits a room-temperature quantum efficiency of 32.2% under applied voltage bias of  $-0.6$  V at 3.5 μm without antireflection coating. The photodetector has a broad response for MWIR with a 100% cutoff at 5 μm. A detectivity of  $8.9 \times 10^8$  cm Hz<sup>1/2</sup> W<sup>-1</sup> is achieved at 3.5 μm under applied bias of  $-0.5$  V.

### Acknowledgements

The authors would like to thank Jean-Luc REVERCHON and Philippe BOIS of III-V THALES for their kind help. This work is supported by A\*Star (Grant No. 1720700038), the Ministry of Education (RG177/17), the Economic Development Board

(NRF2013SAS-SRP001-019), and AOARD (FA2386-17-1-0039).

## Compliance with ethical standards

**Conflict of interest** The authors declare that they have no conflict of interest.

## References

- [1] Rogalski A (2010) Infrared detectors, 2nd edn. CRC Press, Boca Raton
- [2] Trigubo AB, Nollmann I, Casanova JR (1992) Bridgman grown Hg<sub>1-x</sub>CdxTe: crystalline quality assessment by X-ray topography. *J Mater Sci* 27:641–645. <https://doi.org/10.1007/BF00554029>
- [3] Gao YZ, Gong XY, Wu GH et al (2011) Uncooled InAsSb photoconductors with long wavelength. *Jpn J Appl Phys* 50:1–4
- [4] Wang D, Lin Y, Donetsky D et al (2012) Unrelaxed bulk InAsSb with novel absorption, carrier transport, and recombination properties for MWIR and LWIR photodetectors. *Infrared Technol Appl XXXVIII*:835312
- [5] Sharabani Y, Paltiel Y, Sher A et al (2007) InAsSb/GaSb heterostructure based mid-wavelength-infrared detector for high temperature operation. *Appl Phys Lett* 90:232106
- [6] Carras M, Reverchon JL, Marre G et al (2005) Interface band gap engineering in InAsSb photodiodes. *Appl Phys Lett* 87:102103
- [7] Tong J, Tobing LYM, Ni P, Zhang DH (2018) High quality InAsSb-based heterostructure n-i-p mid-wavelength infrared photodiode. *Appl Surf Sci* 427:605–608
- [8] Sadovnikov AV, Grachev AA, Beginin EN et al (2017) Voltage-controlled spin-wave coupling in adjacent ferromagnetic-ferroelectric heterostructures. *Phys Rev Appl* 7:014013
- [9] Davies CS, Sadovnikov AV, Grishin SV et al (2015) Generation of propagating spin waves from regions of increased dynamic demagnetising field near magnetic antidots. *Appl Phys Lett* 107:162401
- [10] Sadovnikov AV, Beginin EN, Odincov SA et al (2016) Frequency selective tunable spin wave channeling in the magnonic network. *Appl Phys Lett* 108:172411
- [11] Sadovnikov AV, Davies CS, Kruglyak VV et al (2017) Spin wave propagation in a uniformly biased curved magnonic waveguide. *Phys Rev B* 96:060401
- [12] Maimon S, Wicks GW (2006) nBn detector, an infrared detector with reduced dark current and higher operating temperature. *Appl Phys Lett* 89:151109
- [13] Craig AP, Marshall ARJ, Tian ZB et al (2013) Mid-infrared InAs<sub>0.79</sub>Sb<sub>0.21</sub>-based nBn photodetectors with Al<sub>0.9</sub>Ga<sub>0.2</sub>As<sub>0.1</sub>Sb<sub>0.9</sub> barrier layers, and comparisons with InAs<sub>0.87</sub>Sb<sub>0.13</sub>p-i-n diodes, both grown on GaAs using interfacial misfit arrays. *Infrared Phys Technol* 67:210–213
- [14] Baril N, Brown A, Maloney P et al (2016) Bulk InAs<sub>x</sub>Sb<sub>1-x</sub> nBn photodetectors with greater than 5 μm cutoff on GaSb. *Appl Phys Lett* 109:122104
- [15] Soibel A, Hill CJ, Keo SA et al (2014) Room temperature performance of mid-wavelength infrared InAsSb nBn detectors. *Appl Phys Lett* 105:023512
- [16] Klipstein P, Klin O, Grossman S et al (2011) MWIR InAsSb XB<sub>n</sub> detector (bariodes) arrays operating at 150K. *Infrared Technol Appl XXXVII*:80122R
- [17] Haddadi A, Chevallier R, Chen G et al (2015) Bias-selectable dual-band mid-/long-wavelength infrared photodetectors based on InAs/InAs<sub>1-x</sub>Sb<sub>x</sub> type-II superlattices. *Appl Phys Lett* 106:011104
- [18] Ting DZY, Soibel A, Hill CJ et al (2011) Antimonide superlattice complementary barrier infrared detector (CBIRD). *Infrared Phys Technol* 54:267–272
- [19] Noshu BZ, Bennett BR, Whitman LJ, Goldenberg M (2002) Spontaneous growth of an InAs nanowire lattice in an InAs/GaSb superlattice. *Appl Phys Lett* 81:4452–4454
- [20] Bandara S, Maloney P, Baril N et al (2011) Performance of InAs/GaSb superlattice infrared detectors and dependence on minority carrier lifetime. *Infrared Phys Technol* 54:263–266
- [21] Wei Y, Hood A, Yau H et al (2005) Uncooled operation of type-II InAs/GaSb superlattice photodiodes in the mid-wavelength infrared range. *Appl Phys Lett* 86:233106
- [22] Gautam N, Myers S, Barve AV et al (2012) High operating temperature interband cascade midwave infrared detector based on type-II InAs/GaSb strained layer superlattice. *Appl Phys Lett* 101:021106
- [23] Ariyawansa G, Reyner CJ, Steenbergen EH et al (2016) InGaAs/InAsSb strained layer superlattices for mid-wave infrared detectors. *Appl Phys Lett* 108:022106
- [24] Elies S, Krier A, Cleverley IR, Singer K (1993) Photoluminescence of MBE-grown InAs<sub>1-x</sub>Sb<sub>x</sub> lattice matched to GaSb. *J Phys D Appl Phys* 26:159–162
- [25] Ye H, Ni Q (2016) Effects of the composition of diffusion source on the surface concentration and effective surface diffusivity of Zn in n-GaSb. *J Mater Sci* 51:7300–7308. <https://doi.org/10.1007/s10853-016-0012-7>
- [26] Webster PT, Riordan NA, Liu S et al (2015) Measurement of InAsSb bandgap energy and InAs/InAsSb band edge positions using spectroscopic ellipsometry and photoluminescence spectroscopy. *J Appl Phys* 118:245706

- [27] Fang ZM, Ma KY, Jaw DH et al (1990) Photoluminescence of InSb, InAs, and InAsSb grown by organometallic vapor phase epitaxy. *J Appl Phys* 67:7034–7039
- [28] Chen H, Verheyen P, De Heyn P et al (2016) Dark current analysis in high-speed germanium p-i-n waveguide photodetectors. *J Appl Phys* 119:213105
- [29] Shabani J, McFadden AP, Shojaei B, Palmstrøm CJ (2014) Gating of high-mobility InAs metamorphic heterostructures. *Appl Phys Lett* 105:262105
- [30] Khai LW, Hua TK, Daosheng L et al (2016) Room temperature 3.5- $\mu\text{m}$  mid-infrared InAs photovoltaic detector on a Si substrate. *IEEE Photonics Technol Lett* 28:1653–1656
- [31] <http://www.hamamatsu.com/eu/en/product/category/3100/4007/4143/index.html>. Accessed 14 Jun 2018